

Unified Graph based Multi-Cue Feature Fusion for Robust Visual Tracking

Kapil Sharma, *Senior Member, IEEE*, Himanshu Ahuja, *Student Member, IEEE*, Ashish Kumar, *Member, IEEE*, Nipun Bansal, *Member, IEEE*, and Gurjit Singh Walia, *Senior Member, IEEE*

Abstract—Visual Tracking is a complex problem due to unconstrained appearance variations and dynamic environment. Extraction of complementary information from the object environment via multiple features and adaption to target’s appearance variations are the key problems of this work. To this end, we propose a robust object tracking framework based on Unified Graph Fusion (UGF) of multi-cue to adapt to the object’s appearance. The proposed cross-diffusion of sparse and dense features not only suppresses the individual feature deficiencies but also extracts the complementary information from multi-cue. This iterative process builds robust unified features which are invariant to object deformations, fast motion and occlusion. Robustness of the unified feature also enables the random forest classifier to precisely distinguish the foreground from the background, adding resilience to background clutter. In addition, we present a novel kernel-based adaptation strategy using outlier detection and a transductive reliability metric. The adaptation strategy updates the appearance model to accommodate variations in scale, illumination, rotation. Both qualitative and quantitative analysis of 25 benchmark video sequences (OTB-50, OTB-100 and VOT2017/18) shows that the proposed UGF tracker performs favorably against 15 other state-of-the-art trackers under various object tracking challenges.

Index Terms—Visual tracking, Adaptive Appearance Model, Feature Fusion, Outlier Detection

I. INTRODUCTION

TRACKING objects in video sequences have emerged as one of the most challenging problems in the field of computer vision. Generally, object tracking framework aims at keeping track of the targeted object in subsequent frames while catering to various tracking challenges. The challenges in object tracking arise due to changes in object appearance such as its deformation, scale variations, fast motion, and in-plane and out-of-plane rotation, and due to a dynamic environment such as illumination variations, occlusion and background clutter. Despite this, object tracking has been investigated extensively due to its wide range of applications viz. military surveillance, robotics, medical imaging, augmented reality and human-computer interaction.

Recently, multi-cue based object tracking solutions have been investigated and reviewed [1]. Typically, multi-cue based trackers consider complementary visual cues so that if one cue fades, the other cue can compensate. These trackers can fuse the extracted information at the score or the feature level. Score level approach uses classifier scores for segmentation of target from the background. Multiscale spatio-temporal context tracker [2], and hash tracker [3] considered score level fusion. On another hand, feature level fusion combines different feature vectors extracted from individual cues.

Lan *et al.* [4] used a sparse representation for feature level fusion to remove unreliable features dynamically. In [5], color and HOG features are considered for object representation. Generally, trackers based on feature-level fusion fail to capture the non-linear variations in illumination, deformations, and occlusion of the targeted object due to off-course updating of the tracker. Despite recent investigations in this direction, adaptive non-linear feature fusion for building a robust appearance invariant to dynamic environment remains a challenge.

Tracker’s appearance model keeps a record of the visual changes in the object, and hence its design plays a critical role in tracker’s overall success. Generally, appearance models are classified as generative and discriminative models. Generative models consider only foreground information but ignore background information for target representation. Generative models have been exploited for building trackers such as DFT [6] and ASLA [7]. On the other hand, discriminative trackers separate the target from the background and consider tracking as a binary classification problem. Trackers such as MIL [8], STRUCK [9] and CT [10] were presented under the discriminative model. Discriminative trackers assume the background and foreground to have a linear relationship. However, this condition does not hold true in real-world scenarios. Generally, trackers based on generative model tend to drift in large search space, background clutters, occlusion and large variations in target appearance, whereas, trackers based on the discriminative model are more robust and reliable to these variations. However, the success of discriminative models is highly dependent on the selection of training samples and the optimal design of the updating strategy. Alternatively, many deep learning based trackers have been proposed [11]–[13] to model target’s appearance. Although these models can automatically discover feature representation for the targeted object, they require extensive pre-training and are generally unemployable in real-time scenarios.

In this paper, we propose a real-time object tracking architecture based on unified graph fusion and an adaptive appearance model which exploits the advantages of both discriminative and generative models. The discriminative appearance model is based on outlier detection and fragment distribution to tackle background clutter and occlusions. The unified graph fusion utilizes proposed cross-diffusion based generative process to build robust features invariant to illumination, scale, and deformations. To summarize, the main contributions of this research are as follows:

- We propose an object tracking framework based on unified graph fusion of multiple features, which creates

a highly marginalized decision boundary between feature descriptors of positive and negative fragments. This is achieved through the proposed cross-diffusion algorithm which captures the strong relationships between feature descriptors and suppresses any weak relations, making the tracker invariant to illumination and scale variations. The algorithm iteratively fuses sparse and dense similarity graphs and performs recursive normalization for faster convergence.

- We propose an outlier detection mechanism based on the proximity of a candidate fragment to positive and negative class samples. The proximity measure evaluates the nodes of the decision trees in the random forest, where the candidate fragment lands. This ensures that the updating of the classifier does not compromise its accuracy. In addition, it enhances the selection of fragments for precise localization of the targeted object. This not only makes the tracker resistant to background clutter but also ensures efficient training of the classifier during initialization and updating of the appearance model.
- We propose a novel adaptive appearance model to preserve temporal and spatial consistency and tackle deformations and pose variations. The mechanism distributes the proximal candidate fragments based on classifier confidence scores and sample reliability using multi-class SVM. The reliability metric prevents the appearance model to be updated with fragments containing background clutters and ensures that the updating samples do not overfit the classifier. Using regular updates for a robust and dynamic appearance model and periodic updates of reference templates prevents eventual drift in long video sequences.

The rest of this paper is organized as follows: In Section II, we closely review the literature to gauge the research gap. In Section III, we present the architecture of the proposed UGF Tracker. In Section IV, we perform experimental validation and compare our tracker with 15 other state-of-the-art trackers over 25 benchmarked video sequences. Finally, concluding remarks and future directions are sketched in Section V.

II. RELATED WORK

Visual Tracking has been rigorously investigated over the last decade. Generally, the performance of any visual tracking solution depends on building a robust and dynamic appearance model. In this section, we examine closely related object appearance models and their adaptation strategies to dynamic environment.

Mostly, generative models represent target’s appearance using foreground information. In this direction, many sparse based methods [14]–[16] were proposed. In [14], authors proposed weighted local sparse representation to measure the importance of each patch. The adaptive template update strategy considered incremental subspace and sparse coding for each reliable patch. On the other hand, in [16], appearance characteristics of the local patch was categorized as stable, invalid and valid with an importance weighting. A discriminative local sparse coding was used to separate the background patches from stable ones and a linear regressor was used to separate

the invalid patches from valid patches. Xue *et al.* [2] exploited three types of spatial-temporal context information for long, medium, and short term components during visual tracking. Visual spatial information was used for sample selection. Chen *et al.* [15] used frame difference masks to encode large-scale corruption information into a modulated dynamic sample dictionary. Hu *et al.* [17] exploited structure-aware local sparse coding for encoding each candidate sample. In this, encoding samples were reduced by using global sparsity constraint on coding coefficient. Generally, sparse based generative methods cannot handle many of the tracking challenges due to lack of background discriminative information.

On the other hand, discriminative appearance models separate the target from the background. In this direction, Huang *et al.* [18] proposed a part-based discriminative model wherein object appearance was constructed using a supervised descent method with two online reliabilities. For catering appearance variations, the updating model was made adaptive through incremental cascaded support vector regression. In [19], authors proposed to integrate subspace information and intrinsic geometric structures among tasks using dual-graph regularized discriminative multitask low-rank learning. Du *et al.* [20] used association and geometric encoding functions to compute the confidence of part-sets in a hypergraph. A mode-seeking function selected the most-probable parts over a candidate set. In addition, many correlation filter based appearance model were also proposed [21]–[23]. Hu *et al.* [21] proposed elastic net constraint with correlation filter to handle the tracking challenges. In this, peak strength metric was defined to improve the capability of the filter. In [23], instead of a metric, the authors used an iterative graph-seeking strategy which minimizes an energy function based on correlation filters. Hu *et al.* [22] proposed the manifold regularization in correlation filter for unlabelled data and sample space. The tracker in [5] jointly treats the visual and geometric properties within a single formulation, with correlation filter at the coarse-level and a color model to localize the object.

Recently, many deep learning based trackers [24]–[26] were proposed pertaining to their favorable performance to model the target’s appearance. In [24], authors considered the problem of visual tracking as a trajectory estimation task using convolutional and recurrent units. A large training data is required to predict trajectories, which is often unavailable. In [13], author exploited part context information and importance reliability to preserve target’s spatial information using deep regression. In [12], authors used a Siamese network with on-line adaptive hedge algorithm for similarity measure between the target and weak experts based on CNN layer. Similarly, Gao *et al.* [11] train a Siamese neural network to construct a structural relationship between image patches. Mostly, deep learning based visual trackers require pre-training of the neural network on a large auxiliary image dataset. To overcome pre-training, Zhang *et al.* [26] initialize random convolutional filters and only train the fully connected layer. Even then, deep-learning based trackers could not be used in real-time scenarios and employ computationally intensive fine-tuning.

Review of the closely related literature indicates that future research direction should consider the design of a robust ap-

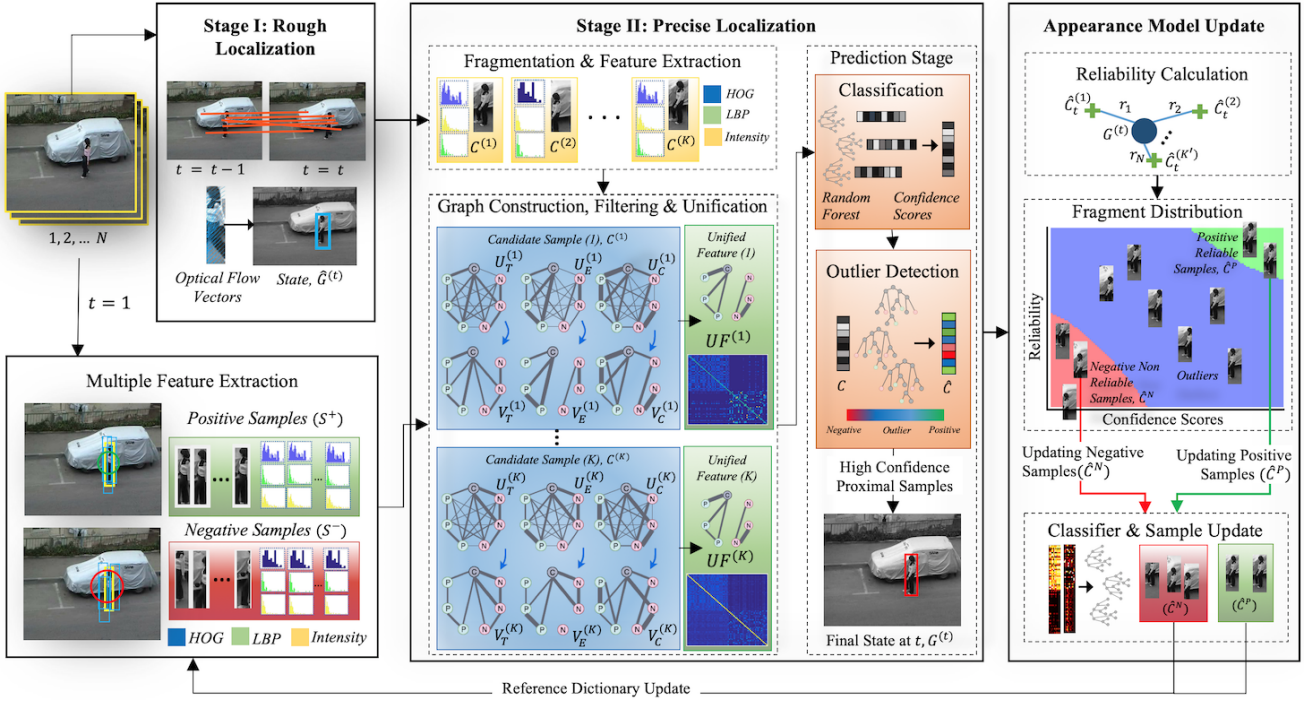


Fig. 1. Overview of the UGF Tracking algorithm. The model is initialized ($t = 1$) by generating unified features for positive and negative fragments based on the proposed cross-diffusion algorithm. For each prediction step, $t = (2, 3, \dots, N)$, the appearance model adapts to the current object environment based on an outlier detection mechanism and fragment distribution strategy considering classifier confidence scores and a transductive reliability metric.

pearance model using multiple features with an online adaptive updating strategy, regardless of whether it is generative or discriminative. The next section details UGF's methodology.

III. PROPOSED METHODOLOGY

The proposed UGF Tracker leverages both motion cues and visual descriptors for precise localization of object in video sequence. To adapt to variations in the object environment, the proposed tracker uses a robust updating strategy encompassing a proximity-based outlier detector, a transductive reliability metric and, classifier confidence scores. The appearance model of the object is based on the proposed cross-diffusion of HOG (F_e), LBP (F_t) and Intensity (F_c) feature descriptors. The direct fusion of features is vulnerable to small changes in object appearance, hence, we use feature scores to calculate the fused feature descriptors of the given fragments. Fig. 1 illustrates the appearance model, object localization and updating strategy of the UGF Tracker. At $t = 1$, the architecture is initialized by sampling positive (S^+) and negative (S^-) fragments around the target object. This is followed by construction of unified feature descriptors $UF_T(C^{(k)})$ from dense (U_e^k, U_c^k, U_t^k) and sparse (V_e^k, V_c^k, V_t^k) adjacency matrices of each candidate fragment, $C^{(k)}$. These fragments are fed to a random forest classifier (\mathcal{R}) for training and are stored for construction of fused descriptors of candidate fragments during the prediction stage. The object localization during the prediction stage ($t = 2, 3, \dots, N$) is a two-fold process. At each time step t , an initial rough localization using optical flow, \tilde{G}_t provides a more effective sampling state than G_{t-1} for feature extraction. Multiple extracted features of each candidate fragment are then

fused using graph unification. The fused feature descriptors are fed to a two-phase classifier, which first classifies the positive and negative fragments followed by a secondary outlier detector which finds borderline positive and negative predictions, \hat{C} , using class proximity measure based on leaf node count. The final target location, G_t , is obtained using softmax probability of the positive fragment centroids. Further, at each time step, a transductive reliability metric, $(r(\hat{C}^{(k)}))$, is evaluated for each fragment. The reliability along with confidence score of proximal fragments is used for fragment distribution based on multi-class SVM. The positive (\hat{C}^P) and negative (\hat{C}^N) reliable fragments from this distribution are then fed to the classifier. The reference dictionary is also updated by selective replacement with positive and negative reliable fragments. This ensures that the classifier temporally adapts to the changes in object appearance.

A. Stage I: Rough Localization

In the first stage of object localization, the tracker evaluates motion cues from the apparent movement of pixel intensity values between consecutive frames. In the proposed architecture, we utilize the Horn-Schunk Optical Flow method [27] for rough estimation of the target centroid in the subsequent frame. The method estimates the change in pixel intensity $\mathcal{I}(x, y, t)$ at time t , by assuming that the illumination variation between consecutive frames is zero. Using this assumption, we get Eq. (1) wherein the spatial gradient of intensity is represented by \mathcal{I}_x & \mathcal{I}_y . \mathcal{I}_t represents the change in intensity w.r.t time, and u and v represent the estimation of the velocity field.

$$\mathcal{I}_x u + \mathcal{I}_y v + \mathcal{I}_t = 0 \quad (1)$$

Assuming the smoothness constraint, velocities u and v are derived by minimising the total error (\mathcal{E}_T) using Eq. (2).

$$\mathcal{E}_T = \int \int (\mathcal{I}_x u + \mathcal{I}_y v + \mathcal{I}_t)^2 + \epsilon^2 \left(\left(\frac{\partial u}{\partial x} \right)^2 + \left(\frac{\partial u}{\partial y} \right)^2 + \left(\frac{\partial v}{\partial x} \right)^2 + \left(\frac{\partial v}{\partial y} \right)^2 \right) dx dy \quad (2)$$

where ϵ^2 scales the smoothness constraint. We select N optical flow vectors in the region surrounding the target centroid, G_{t-1} . The roughly estimated centroid \tilde{G}_t in the current frame is then given by Eq. (3).

$$\tilde{G}_{t,(x,y)} = G_{t-1,(x,y)} + \frac{1}{N} \sum_{i=1}^N (u^{(i)}, v^{(i)}) \quad (3)$$

This \tilde{G}_t is used for generating candidate fragments in the current frame for precise localization of the target centroid.

B. Stage II: Precise Localization

The precise localization of the target is achieved via a multi-cue based recursive graph fusion and normalization technique. Firstly, we sample the fragments, $C^{(k)} \in \{C^{(1)}, C^{(2)}, \dots, C^{(K)}\}$, through a random walk around \tilde{G}_t . Each random walk is associated with the distance from \tilde{G}_t , a scale factor, and an angular displacement. For each candidate fragment, three complementary features are extracted and fused using the proposed cross-diffusion method.

1) *Feature Extraction*: The appearance characteristics of each candidate fragment, $C^{(k)}$ are described by its Histogram of Orientation Gradients (HOG), Local Binary Patterns (LBP) and RGB Histogram (Intensity) feature descriptors. We use these feature descriptors due to their complementary nature which is exploited using the proposed method. The intensity histogram requires less computation load, is invariant to scale and robust to partial occlusions. The intensity histogram of the k^{th} candidate fragment are defined as $F_c^k = \{H_1, H_2, \dots, H_{N_b}\}$ where the binning function assigns each pixel (x_k, y_k) to one of the N_b bins.

LBP feature descriptors are invariant to rotations, handling any in-plane and out-of-plane rotations. LBP operator is determined using Eq. 4.

$$LBP_{\beta, N_p} = \begin{cases} \sum_{j=0}^{N_p-1} u_\epsilon (\mathcal{I}_g^j - \mathcal{I}_g^c), & U(LBP_{\beta, N_p}) \leq 2 \\ p + 1, & \text{otherwise} \end{cases} \quad (4)$$

The texture uniformity, $U(LBP_{\beta, N_p})$ [28] measures the number of bit-wise transitions of pattern labels. \mathcal{I}_g^j , \mathcal{I}_g^c represent the grey value of the central pixel (c) and the j^{th} pixel respectively. β is the neighborhood radius of the central pixel with N_p equally spaced neighboring pixels. For each candidate fragment, $C^{(k)}$, normalized histograms are determined by mapping the uniformity measure for each pixel as F_t^k .

To describe the shape structure of the candidate fragments, we use the HOG feature descriptors [29] which capture the distribution of edge directions. The target object is divided

into image patches or cells with each cell holding the weighted local one dimensional histogram of gradient vectors over the pixels of the cell. A pixel votes for its orientation bin, as well as its neighboring orientation bins. The bins obtained are L_2 -normalized for better invariance to shading and illumination. The histogram of orientation bins for k^{th} candidate fragment is stored as F_e^k as edge feature cue.

2) *Feature Unification*: Our novel graph unification strategy performs non-linear feature fusion with recursive normalization. This retains a strong representation of the target object and discards any weak features that make the tracker susceptible to changes in the object environment. A set of positive (S^+) and negative fragments (S^-) are stored during architecture initialization ($t = 1$) and updated with reliable fragments in each subsequent frame. During the feature unification procedure, the color (RGB), edge (HOG) and texture (LBP) feature descriptors for each candidate fragment, $C^{(k)}$ are diffused into a single robust feature. For each feature descriptor, $F_\mu^x \in \{F_t^x, F_e^x, F_c^x\}$ of fragment vertex $x \in N = \{C^{(k)}, S^+, S^-\}$, we construct graphs, $U_\mu \in \{U_t, U_e, U_c\}$ with edge weight defined as the likelihood between feature descriptors of two fragment vertices. Between any two fragments $x, y \in N$, we construct the similarity matrix $U_\mu \in \mathbb{R}^{N \times N}$ by calculating the Bhattacharya coefficient from their feature descriptors, Eq. (5).

$$\beta_\mu(x, y) = \sqrt{F_\mu(x) \odot F_\mu(y)} \quad (5)$$

The Bhattacharya coefficient is used to calculate the Bhattacharya distance between the features of the fragments, x and y as follows:

$$B_\mu(x, y) = \sqrt{1 - \beta_\mu(x, y)} \quad (6)$$

We use the likelihood estimation on Bhattacharya distance to calculate the likelihood between two feature descriptors as:

$$U_\mu(x, y) = \frac{1}{\sigma_\mu \sqrt{2\pi}} e^{-\frac{(B_\mu(x, y))^2}{2\sigma_\mu^2}} \quad (7)$$

Where, $\sigma_\mu \in \{\sigma_t, \sigma_e, \sigma_c\}$ represents the cue standard deviation. The adjacency matrix U_μ is formed by calculating the likelihood between each of the N vertices of the graph. This is followed by row-wise normalization of U_μ , Eq. (8). The self-similarity is set to a small constant, ϵ for better distribution of weights among other similar fragments. The first row of the normalized similarity matrix \hat{U}_μ contains the edge-weights corresponding to the candidate fragment, $C^{(k)}$.

$$\hat{U}_\mu(x, y) = \begin{cases} (1 - \epsilon) \frac{U_\mu(x, y)}{\sum_y U_\mu(x, y)}, & x \neq y \\ \epsilon, & x = y \end{cases} \quad (8)$$

From \hat{U}_μ , we derive a sparse vector representation of the candidate fragment $V_\mu^k \in \mathbb{R}^{1 \times N}$, which only keeps the most similar elements and sets the other elements to zero.

$$V_\mu^k = \begin{cases} \hat{U}_\mu(C^{(k)}, y), & \text{if } \hat{U}_\mu(y) \in k\text{-NN}(C^{(k)}) \\ 0, & \text{otherwise} \end{cases} \quad (9)$$

In Eq. (9), $\hat{U}_\mu(y) \in \mathbb{R}^{1 \times N}$ represents the row corresponding to adjacency list of the y^{th} sample.

$$\hat{V}_\mu^k = \frac{V_\mu^k}{\sum_{i=1}^N |V_\mu^k|} \quad (10)$$

We normalize the derived vector representation, \hat{V}_μ^k , Eq. (10). This eliminates weak positive and negative relationships from the adjacency list of the candidate fragments. The normalization distributes the weights amongst the strong connections and hence builds a robust sparse representation. To fuse the individual feature sparse vectors, \hat{V}_μ^k , into a single robust feature descriptor $UF_T(C^{(k)}) \in \mathbb{R}^{1 \times N}$, we propose cross-diffusion strategy adapted from [30] for $M = |F_\mu|$ feature descriptors as:

$$U_{\mu,t+1}(C^{(k)}) = \hat{V}_{\mu,t}^k \times \left(\frac{1}{M-1} \sum_{j=1, j \neq \mu}^M \hat{U}_{j,t}(C^{(k)}) \right) \times \hat{V}_{\mu,t}^k \quad (11)$$

To increase computational efficiency of the diffusion process, we modified the iterative process by normalizing the the row corresponding to the candidate sample in the similarity matrix, $U_{\mu,t+1}(C^{(k)}) \in \mathbb{R}^{1 \times N}$, obtained after each iteration as:

$$\hat{U}_{\mu,t+1}(C^{(k)}) = \frac{U_{\mu,t+1}(C^{(k)})}{\sum_{i=1}^N |U_{\mu,t+1}(C^{(k)})|} \quad (12)$$

Based on this new normalized adjacency list of $C^{(k)}$, we find its k -Nearest Neighbours from the original similarity matrix, Eq. (9). Once the weak connections are eliminated, we normalize the sparse vector $V_{\mu,t+1}^k$ to obtain the normalized sparse vector $\hat{V}_{\mu,t+1}^k$ for the next iteration. Finally, the adjacency list of the candidate sample for each feature descriptor, $\hat{U}_{\mu,t}(C^{(k)})$ is averaged to obtain the unified feature $UF_T(C^{(k)})$ by Eq. (13), which will be used as input to the classifier for prediction.

$$UF_T(C^{(k)}) = \frac{1}{M} \sum_{j=1}^M \hat{U}_{j,T}(C^{(k)}) \quad (13)$$

Here, T represents the final iteration of the cross-diffusion normalization process. Figure 2 illustrates the efficiency of our algorithm against previously developed cross-diffusion algorithms. Each row represents the unified feature of the candidate fragment, $UF_T(C^{(k)})$. The first 50 columns describe the similarity scores with positive fragments (S^+) and the next 50 columns represent the similarity scores with negative fragments (S^-). Further, for tracker validation, we take the first 200 candidate fragments to be positive and the next 200 fragments to be negative. Cross Diffusion algorithm [30] in Fig. 2(c) produces almost similar unified features for both negative and positive candidate fragments making training of the classifier inefficient. This is due to unstable self-similarity definition and lack of a normalization procedure during iterative cross-diffusion. An improvement was proposed in [31] by normalization of dense similarity matrix at each iteration. In Fig.2(b) a high self-similarity constant in $U_\mu(C^k)$ reduces the distribution scores amongst other fragments, producing identical unified features for the positive candidate fragments.

Algorithm 1: Proposed Cross Diffusion

```

1 Function GraphFusion ( $C, S^+, S^-, \sigma$ ):
2   for ( $C^{(k)} \in C$ ) do
3      $N \leftarrow [C^{(k)}, S^+, S^-]$ 
4     for ( $F_\mu \in \{F_t, F_c, F_e\}$ ) do
5       derive  $U_\mu$  from Eq. (7) on  $N$ 
6       normalize  $U_\mu$  to  $\hat{U}_\mu$  using Eq. (8)
7       if  $\hat{U}_\mu(y) \in k\text{-NN}(C^{(k)})$  then
8          $V_\mu^k \leftarrow \hat{U}_\mu(C^{(k)}, y)$ 
9       else
10         $V_\mu^k = 0$ 
11      end
12      normalize  $V_\mu^k$  to  $\hat{V}_\mu^k$  using Eq. (10)
13      repeat
14        find  $U_{\mu,t+1}(C^{(k)})$  using  $\hat{U}_{\mu,t}(C^{(k)})$  and
15         $\hat{V}_{\mu,t}^k$  from Eq. (11)
16        normalize  $U_{\mu,t+1}(C^{(k)})$  to  $\hat{U}_{\mu,t+1}(C^{(k)})$ 
17        using Eq. (12)
18         $\hat{U}_{\mu,t}(C^{(k)}) := \hat{U}_{\mu,t+1}(C^{(k)})$ 
19      until convergence
20      end
21      find  $UF_T(C^{(k)})$  using  $\hat{U}_{\mu,T}(C^{(k)})$  from Eq. (13)
22 end
23 return  $\{UF_T(C^{(1)}), UF_T(C^{(2)}), \dots, UF_T(C^{(K)})\}$ 

```

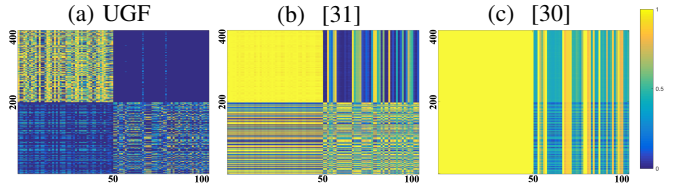


Fig. 2. Feature descriptors constructed using Bhattacharya similarity metric (a) Proposed Cross-Diffusion (b) Modified Cross-Diffusion [31] (c) Cross-Diffusion [30]

This method also produces anomalies, by describing negative candidates as positive. In the proposed method, the introduction of recursive normalization of dense similarity matrix and vector sparse representation with an optimized self-similarity score leads to better distribution of similarity scores amongst other fragments. The recursive formation of \hat{V}_μ^k from $U_{\mu,t}(C^{(k)})$ highlights strong connections and diminishes the weaker connections unlike [31] and [30] which use the same sparse matrix in each iteration. Algorithm 1 summarized the procedure of the proposed cross diffusion method.

3) *Prediction Stage*: The evaluation of prediction for precise localization is a two-fold process. At each time step $t = (2, 3, \dots, N)$, the random forest classifier (\mathcal{R}) assigns each input feature vector $UF(C^{(k)})$ of candidate sample $C^{(k)}$, a prediction score. We adopted the bagging algorithm from Breiman [32] which creates a single strong classifier from many weak classifiers. Each candidate feature is assigned a value in $[0, 1]$ according to its resemblance to the positive and negative fragments encountered during training of the

classifier. At end of this stage we get a set of K scores for frame t , $\Delta_t = \{\delta_1, \delta_2, \dots, \delta_K\}$. Next, we evaluate the proximity of the candidate sample, $C^{(k)}$ towards a class as the proportion of decision trees, $\mathcal{R}_t \in \mathcal{R} = \{\mathcal{R}_1, \mathcal{R}_2, \dots, \mathcal{R}_T\}$, for which $C^{(k)}$ falls on the same leaf node (\mathcal{R}_t^l) versus other candidate fragments that fall in the same class, Eq. (14). For a particular class, proximity (p) is defined by Eq. (15).

$$\hat{p}(C^{(k)}, C^{(j)}, \mathcal{R}_t) = \begin{cases} 1, & \text{if } \mathcal{R}_t^l(C^{(k)}) = \mathcal{R}_t^l(C^{(j)}) \\ 0, & \text{otherwise} \end{cases} \quad (14)$$

$$p(C^{(k)}) = \frac{1}{T} \sum_{t=1}^T \sum_{k=1, k \neq j}^K \hat{p}(C^{(k)}, C^{(j)}, \mathcal{R}_t) \quad (15)$$

Any $C^{(k)}$ with low proximity to their predicted sample class are considered outliers and are discarded to get the proximal candidate dictionary, $\hat{C} = \{\hat{C}^{(1)}, \hat{C}^{(2)}, \dots, \hat{C}^{(K')}\}$. The high confidence, proximal candidate fragments are averaged by the softmax probability of their confidence scores, Eq. (16), to get the new precisely located centroid, G_t at time step t , Eq. (17).

$$\alpha_k = \frac{e^{\delta_k}}{\sum_{j=1}^{K'} e^{\delta_j}} \quad (16)$$

$$G_t = \sum_{k=1}^{K'} \alpha_k \hat{C}^{(k)}(x, y) \quad (17)$$

where, $\hat{C}^{(k)}(x, y)$ represents the centroid of the k^{th} candidate sample. Once the target object is localised, we update the appearance model of the object environment for consistent evaluation of subsequent frames.

C. Updating Strategy

To update the classifier, \mathcal{R} at each time step, we consider the proximal, high confidence and low confidence fragments and calculate their reliability. The random forest classifier contains a bag of regression trees. Each of these decision trees vote on the candidate fragment based on their branching structure. The fact that a simple bag of regression trees is able to give high accuracy can be leveraged to distinguishing robust unified feature vectors. Further, the reliability metric $r(\hat{C}^{(k)})$ is used as a label of confidence for each selected fragment as:

$$r(\hat{C}^{(k)}) = a \times (\tanh(-\|\hat{C}^{(k)} - G_t\|_2 + b) + c) \quad (18)$$

Here, a, b and c are constants that describe the shape of the hyperbolic tan function. We derive a fragment distribution decision model, based on *one-vs-one* multi-class SVM, dividing the proximal candidate fragments into three categories: high confidence fragments with high reliability (\hat{C}_P), high confidence, low reliability or low confidence, high reliability fragments labelled as outliers (\hat{C}_O) and low confidence, low reliability fragments (\hat{C}_N). Each data point, $\mathbf{x}_k = (r(\hat{C}^{(k)}), \delta_k)$, is represented as a pair of sample reliability and its confidence score. Each \mathbf{x}_k is mapped to a $y_k \in \{\hat{C}_P, \hat{C}_N, \hat{C}_O\}$ for formulating the fragment distribution during initialization. For a pair of classes, $i, j \in \{\hat{C}_P, \hat{C}_N, \hat{C}_O\}, i \neq j$, \mathbf{w}^{ij} is chosen to minimize the objective function as a binary classification

problem, for a penalty factor, C and ξ_k^{ij} for relaxation from misclassified fragments as follows:

$$\begin{aligned} & \text{minimize } \frac{1}{2} \|\mathbf{w}^{ij}\|^2 + C \sum_{k=1}^{K'} \xi_k^{ij}. \\ & \text{subject to } \begin{cases} \mathbf{w}^{ij} \cdot \mathbf{x}_k + b^{ij} \geq 1 - \xi_k^{ij}, & \text{if } y_k = i \\ \mathbf{w}^{ij} \cdot \mathbf{x}_k + b^{ij} \leq -1 + \xi_k^{ij}, & \text{if } y_k = j \\ \xi_k^{ij} \geq 0 \end{cases} \end{aligned} \quad (19)$$

Using the *kernel trick* [33], we map the data to a non-linear space for better generalization during prediction. The results for the linear, Gaussian and polynomial kernel for sample classification are depicted in Fig. (3). The RBF kernel, \mathcal{K}_{RBF} ,

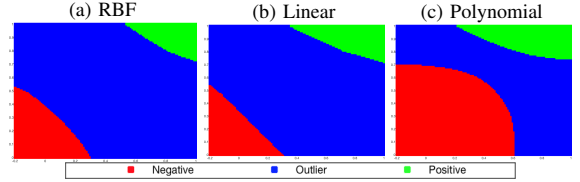


Fig. 3. Various Kernels on multi-class SVM classification for fragment distribution.

Eq. (20), was able to generalise the best on the training data by generating optimal negative and positive class fragments and discarding most fragments as outliers.

$$\mathcal{K}_{\text{RBF}}(\mathbf{x}_i, \mathbf{x}_j) = e^{-\gamma \|\mathbf{x}_i - \mathbf{x}_j\|^2} \quad (20)$$

This ensures a faster and efficient update of the random forest. The decision boundary is solved from a voting strategy wherein each of the M binary classifiers votes for a class on each incoming sample (\hat{C}^k). At each time step, the predicted \hat{C}_P are used as positive samples for updating the classifier, whereas \hat{C}_N from the proximal candidate fragments set, \hat{C} are used as negative samples. The selected candidate fragments along with their respective labels are fed to the random forest, \mathcal{R} for an update. To improve accuracy while tackling long term visual tracking challenges, we also add a secondary periodic re-detection procedure to identify the location of the target object when all candidate fragments are detected to be outliers i.e. when all the sampled fragments are not proximal to either of the two classes. The re-detection strategy utilises simple correlation filter around the previously estimated centroid (G_{t-1}) along with the estimated object trajectory to provide an estimation of the centroid in time step t . This prevents drift of the tracker from the target object due to sudden changes in the object environment. Algorithm 2 describes the adaptation of the appearance model, along with the prediction of target state in each frame. In the following section, we evaluate our tracker's performance against other state-of-the-art trackers.

IV. EXPERIMENTAL VALIDATION

A. Experimental Setup

The appearance model of the proposed tracker is build using complementary multi-cue namely HOG, LBP and RGB histograms. For fragment initialization, the sampling radius is defined to be large enough to capture the targeted object completely with minimal overlap of the fragments. The number of

Algorithm 2: Prediction and Updating Strategy

```

1 Function AppearanceModel ( $G_{t-1}, \mathcal{P}, \mathcal{R}, S^+, S^-$ ):
2    $\hat{G}_t \leftarrow \text{HK-OpticalFlow}(G_{t-1})$ 
3    $C \leftarrow \text{Sampling}(\hat{G}_t, \mathcal{P})$ 
4    $\hat{C} \leftarrow \phi$ 
5   for ( $C^{(k)} \in C$ ) do
6      $\text{UF}_T \leftarrow \text{GraphFusion}(C^{(k)}, S^+, S^-, \sigma)$ 
7      $\delta_k \leftarrow \mathcal{R}(\text{UF}_T(C^{(k)}))$ 
8     find proximity of  $C^{(k)}$  using Eq. (15) & Eq. (14)
9     if  $p(C^{(k)}) < P_{\text{Threshold}}$  then
10      | discard  $C^{(k)}$ 
11     else
12      |  $\hat{C}.\text{append}(C^{(k)})$ 
13     end
14   end
15   find  $\alpha_k$  from  $\Delta = \{\delta_1, \delta_2, \dots, \delta_k\}$  using Eq. (16)
16   find  $G_t$  using  $\alpha_k$  from Eq. (17)
17   for ( $\hat{C}^{(k)} \in \hat{C}$ ) do
18     | find reliability of  $C^{(k)}$  using Eq. (18)
19   end
20    $\text{SVM} \leftarrow \text{SVM Model}(r(\hat{C}), \Delta)$ 
21   for ( $\hat{C}^{(k)} \in \hat{C}$ ) do
22     |  $\{\hat{C}^P, \hat{C}^O, \hat{C}^N\} \leftarrow \text{SVM}(\hat{C}^{(k)})$ 
23   end
24   Replace  $\hat{C}^P$  in  $S^+$  and  $\hat{C}^N$  in  $S^-$ 
25   Update SVM Model with  $\hat{C}^P, \hat{C}^O$  and  $\hat{C}^N$ 
26   Train  $\mathcal{R}$  with  $S^+$  and  $S^-$ 
27   Update sample set with  $\hat{C}^P, \hat{C}^N$ 
28   return  $\mathcal{R}, G_t$ 

```

fragments chosen for initialization significantly depend on the dimensions of the targeted object i.e. a low-resolution target requires fewer samples than a target with high resolution. The tracking parameters used for simulation of the proposed tracker are defined as follows: the size of positive and negative sample dictionary are, $(S^+) = 50$ and $(S^-) = 50$ respectively, the number of candidate sample generated in each frame is, $|C| = 15$, the reliability and prediction thresholds are set, $a = 0.5$, $b = 7$, $c = 0.7$ and $P_{\text{Threshold}} = 0.75$. To compare the proposed tracker with other tracking methods, we used MATLAB 2016b on an i7 2.2GHz machine with 16GB RAM. **The source code of this paper will be made publicly available.**

B. Datasets and Evaluated Trackers

The proposed UGF tracker is evaluated on 25 benchmark sequences from OTB-50, OTB-100 [34] and VOT2017/18 [35] dataset for rigorous performance analysis on various visual tracking challenges. A total of 12544 frames comprising of video sequences from both stationary and moving cameras are used for evaluation. Further details of the challenges and their respective video sequences are tabulated in Table I.

The performance of the tracker is compared against 15 other state-of-the-art trackers. The evaluated trackers are included as: a) Generative trackers (2 trackers): Distribution Fields for tracking (DFT [6]), Adaptive Structural Local sparse appear-

TABLE I
TRACKING CHALLENGES AND VIDEO SEQUENCES

Tracking challenges	Video Sequences
Occlusion & Background clutters (16 Sequences)	Football, Subway, MountainBike, Singer2, CarDark, Crossing, Car24, Bolt2, Basketball, Walking, Jogging1, Jogging2, Walking2, Pedestrian1, Tiger, Soccer1
Scale variations (11 Sequences)	Car24, Walking, Dancer, Walking2, Boy, Dog1, Crossing, Pedestrian1, Soccer1, Singer1, Shaking
Illumination Variations (9 Sequences)	Singer2, CarDark, Fish, Car24, Basketball, Tiger, Singer1, Shaking, Soccer1
Deformations & Fast motion (12 Sequences)	Walking, Subway, Jogging1, Jogging2, Dancer, Singer2, Crossing, Bolt2, Basketball, Pedestrian1, Soccer1, Bolt1
In-plane Rotation (10 Sequences)	Surfer, Boy, Singer2, Football, MountainBike, Dancer, Dog1, Shaking, Bolt, Tiger
Out-of-plane Rotation (15 Sequences)	Surfer, Boy, Crossing, Singer2, Football, MountainBike, Dancer, Dog1, Basketball, Jogging1, Jogging2, Pedestrian1, Singer1, Shaking, Bolt1

ance based tracker (ASLA [7]), b) Discriminative trackers (8 trackers): Multiple Instance Learning (MIL [8]), Structured output tracker (Struck [9]), Compressive Tracker (CT [10]), Weighted Multiple Instance Learning (WMIL [36]), Incremental Discriminative Color learning Tracker (IDCT [37]), fast Discriminative Scale Space Tracking (fDSST [38]), Learning Continuous Convolution Operators for Visual Tracking (CCOT [39]), Multiple Experts using Entropy Minimization (MEEM [40]), c) Correlation filter based trackers (4 trackers): Discriminative Correlation Filter with Channel and Spatial Reliability (CSRT [41]), Attentional Correlation Filter Network for Adaptive Visual Tracking (ACFN [42]), Context-Aware Correlation Filter Tracking (DCF-CA [43]), Kernelized Correlation Filter (KCF [44]), d) Hybrid tracker (1 tracker): Sparsity-based Collaborative Model based tracker (SCM [45]). Among these trackers, CCOT and MEEM are based on CNN and entropy minimization respectively. Also, CCOT is the winner of the VOT2016 challenge.

C. Evaluation Metrics

Four performance metrics are considered for quantitative analysis: centre location error (CLE), F-measure, distance threshold vs precision plot and success rate vs overlap threshold plot [34]. CLE is described as the Euclidean distance between target bounding box and the ground truth. ORE (Accuracy) is defined as $\Delta(\text{BB}_t \cap \text{BB}_g) / \Delta(\text{BB}_t \cup \text{BB}_g)$, where BB_t is target bounding box and BB_g is ground truth bounding box. F-measure is calculated as the harmonic mean of precision (P) and recall (R). Precision is defined as the overlap of BB_t and BB_g with respect to BB_t and recall determined by the overlap of BB_t and BB_g in reference to BB_g . Precision plots represent the mean precision at various centre error thresholds (in pixels). The Success plot illustrates the percent success over various overlap thresholds (in %). Overlap precision is the percentage of frames where bounding box overlap is above a threshold.

D. Challenge-based Evaluation

In this section, we analyze and compare the performance of trackers under six tracking challenges for video sequence as described Table in I. Trackers output for challenging frames of the benchmark video sequences are illustrated in Fig. 4.

1) *Object Deformation and Fast Motion*: Generally, deformation in target appearance can occur due to pose variations



Fig. 4. Tracking results on critical frames for selected benchmark video sequences. The frame # and the name of the sequence are shown on the top left and right corner respectively of each frame.

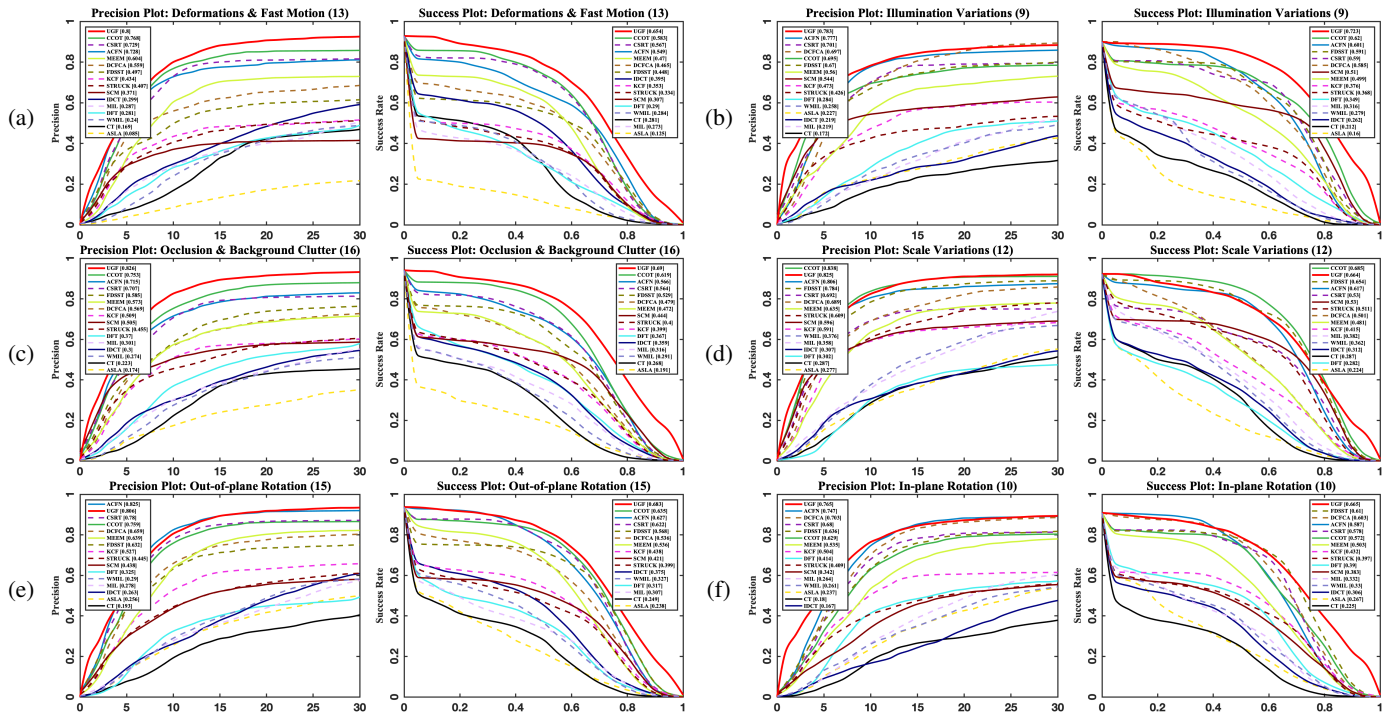


Fig. 5. Precision plots and Success plots for six visual tracking challenges namely deformations, illumination variations, occlusion and background clutter, scale variation, out-of-plane rotation and in-plane rotation. The legend ranks the trackers for each challenge, using the area under curve (AUC) for the success plot, and the score at 10px threshold for the precision plot.

or background clutter. In *Pedestrian1* sequence, there is a considerable change in the appearance of the targeted object, along with rapid camera movements. Ours, ACFN, MEEM, CCOT, and IDCT successfully keep track of target throughout the whole sequence. The regular update of the tracker with reliable high confidence candidate fragments keeps track of the dynamic object environment. Generation of robust complementary features through the proposed cross diffusion exploits LBP and RGB features over HOG as it deteriorates with

deformations. *Bolt2*, *Tiger* sequence, is full of pose variations. Most trackers fail as their appearance model is vulnerable to rapid change in object appearance except ours, CCOT, DFT and CSRT. In *Basketball* and *Jogging1*, generative trackers viz. ASLA and DFT drifted from the target as they consider erroneous background pixels as the target. The *Jumping* sequence contains high object deformation, fast motion and motion blur. The eventual erroneous update of the proposed tracker with blurred fragments results in a comparatively

lower performance in MIL, but higher performance than other trackers due to periodic update. As illustrated in Fig. 5 (a), UGF achieved an average precision score of 0.8 and an average success score of 0.654.

2) *Illumination Variations*: Sudden and considerable illuminations variations are observed in *Singer2* and *Fish* where ours, KCF, DCFCFA, ACFN and CCOT outperform other trackers. This is because the appearance model is built, with a considerably higher number of fragments compared to the incoming fragments. In *CarDark* and *Crossing*, the non-linear multi-cue fusion of feature descriptors builds a robust representation of the object, making the tracker invariant to eventual changes in illuminations. Here, the HOG feature descriptor suppresses the inconsistencies in RGB and LBP cues, which are susceptible to change in illumination. In *CarDark*, ACFN, MIL, and CT fail to build a robust target representation under low-contrast setting leading to eventual drift in these sequences. Our tracker shows comparatively low performance to SCM and CCOT on *Car24* due to fragment updates having minor background clutter after ≈ 1500 frames. The average precision score of 0.783 and average success score 0.723 of is attained by UGF as shown in Fig. 5(b), outperforming all other trackers.

3) *Occlusion and Background clutters*: In *MountainBike*, *Walking* and *Soccer1*, the target shows similar texture to that of the background. Ours with CSRT, CCOT and MEEM is able to handle background clutter. The rest of the trackers show minor drifts caused by eventual inconsistent updates. In *Football* sequence at frame #153, when the target is surrounded by other players, only the proposed approach, CCOT, ACFN, CSRT, DFT, fDSST, and SCM successfully keep track of the object, while DCFCFA and MEEM are susceptible to clutter. This owes to the outlier detection mechanism which eliminates the non-reliable high confidence fragments during an update, keeping the appearance model robust. Further, during partial occlusion of the targeted object, the inherent selective boosting of LBP and RGB features and suppressing of HOG feature descriptors by proposed cross diffusion algorithm ensures precise localization. Target has been occluded by other persons in subsequent frames (#47 and #150) of the *Subway* sequence. ASLA, WMIL, MEEM, and fDSST failed to recover under occlusion as there is no drift alleviation mechanism in them but ours with CCOT, ACFN, and KCF is able to cater to the drifts. Similarly, in *Jogging2* when the target is occluded by the pillar, all but ours, CSRT, SCM, CCOT and ACFN lose the targeted object. Under this challenge, UGF outperformed the other trackers with an average precision score of 0.826 and average success score of 0.69 as depicted in Fig. 5(c).

4) *Scale Variations*: To evaluate the proposed algorithm's scale adaptation methodology, we test UGF on 8 video sequences. In *Walking2*, WMIL, ASLA, CT, DCFCFA, MIL, MEEM, CSRT and IDCT lose the target object to a similar occlusion due to inefficiency in handling variations in scale. At #421, ours, CCOT, SCM and ACFN are efficiently able to adjust to target's scale variation whereas the appearance model in MEEM, KCF, ASLA, DFT, fDSST and STRUCK gets corrupted by background clutter as the size of the targeted

object reduces. SCM, MIL and IDCT suffer in the sequences, *Dancer*, *Surfer*, *Boy* and *Shaking* where scale variations are accompanied by in-plane and out-of-plane rotations. Our method's periodic and regular updating strategy accompanied by complementary fusion of multi-cue accommodates various possible appearance of the object sampled at various scales, hence shows high performance as compared to other trackers. Under this challenge, as shown in Fig. 5(d), the proposed tracker achieved the second highest average precision score of 0.825 and second highest average success score of 0.664.

5) *Out-of-plane rotation*: These occur in sequences where the target object moves out of the image plane. In *Dog1* and *Dancer*, and *Singer2*, out-of-plane rotation and scale variations are tackled via UGF by amplifying the LBP, and HOG feature descriptors over RGB. Under such settings, ours, IDCT, MEEM, and KCF were able to tackle variations and efficiently track the target object. In *Singer2*, #304, CCOT and MEEM among many other trackers fail to keep track the target object. UGF handles out-of-plane rotations with background clutter in sequences *Football*, *MountainBike* and *BasketBall*, *Shaking* by consistently updating the online dictionary. Under this challenge, UGF achieved an average precision of 0.806 after ACFN and an average success of 0.683 (Fig. 5(e)).

6) *In-plane rotation*: Frequently occur in image sequences due to rotation of target in the image plane. In *MountainBike* and *Surfer*, the target objects undergo substantial amount of in-plane rotations throughout the sequence. UGF is able to handle eventual changes in orientation of the target object by regularly updating the sample dictionary. DFT, CT, IDCT and SCM are not able to interpret the change in orientation of target object and hence loose accuracy. In *Singer1*, *Boy*, *Dancer* and *Dog1*, in-plane rotations are coupled with scale variations which are tackled via the LBP feature descriptors in multi-cue feature extraction. In such scenarios, generative trackers fail due to erroneous updates of negative background samples. The proposed tracker shows maximum precision and success score against other trackers. An average precision score of 0.765 and average success score of 0.665 is attained by UGF (Fig. 5(f)).

E. Computational Complexity Analysis

The major computational load of the proposed tracker is in the cross diffusion step wherein the sample dictionary is updated with positive reliable samples (\hat{C}_P), which involves multiple matrix multiplications and normalization operations (Algorithm 1: Line 14). The proposed cross-diffusion reduces the complexity of the original cross-diffusion from $\mathcal{O}(i \cdot N^4)$ to $\mathcal{O}(i \cdot N \cdot \hat{C}_P^2 + i \cdot N^2)$, where N is the size of the sample dictionary and i describes the number of iterations till convergence. Also, the number of iterations is reduced as the proposed cross-diffusion algorithm converges faster. To evaluate the computational demand of UGF, we have compared the proposed tracker against the other top 5 trackers in terms of speed (frames per second) as illustrated in Table II.

An efficient tracker needs to balance the trade-off between accuracy and speed. Fig. 6 describes a scatter plot to illustrate this trade-off. CSRT, fDSST and DCFCFA show competitive performance to UGF considering the trade-off

TABLE II
FPS COMPARISON OF TOP 6 TRACKERS

Algorithm	CCOT	ACFN	DCFCA	fDSST	CSRT	Ours
Accuracy	0.584	0.613	0.665	0.685	0.701	0.748
Speed (FPS)	0.48	12.2	80.9	60.3	35.9	15.3

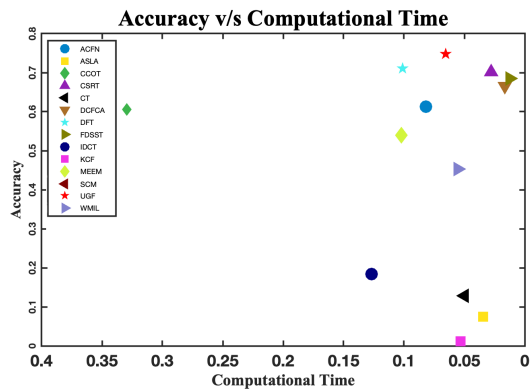


Fig. 6. Scatter plot for Accuracy v/s Computational Time (seconds) on various trackers. Tracker placed on the top right corner correspond to efficient performance, both in computational time and accuracy.

between computational time and accuracy. Although ACFN’s and CCOT’s performance falls close with UGF, the proposed tracker is $\approx 90\%$ faster than CCOT, and $\approx 20\%$ faster than ACFN. Hence, achieves better accuracy with a favorable computational demand against state-of-the-art trackers.

F. Overall Performance

The proposed tracker outperforms the compared state-of-the-art trackers CSRT, fDSST, DCFCA, ACFN, CCOT, MEEM and MIL by 6.22%, .842%, 11.08%, 18.07%, 21.87%, 27.87%, 48.91% respectively in terms of accuracy.

Table III and Table IV, describe the mean CLE and F-Measure of the trackers, respectively. Our proposed tracker achieved an average CLE of 5.01 and an average F-Measure of 0.829 when evaluated on 12554 frames. In sequences with background clutter, occlusion and in-plane and out-of plane rotation, the superior performance of our tracker illustrates the effectiveness of the multi-fold adaptive appearance model which regularly updates the object appearance. The high overlap during illumination and scale variations validate the robustness of the fused feature descriptor against variations in scale and minor changes in object environment. In object deformations and partial occlusion, the complementary feature cues generated via the proposed cross-diffusion ensured high precision by exploiting effective visual cues over deteriorating ones. The proposed method significantly improves over existing fragment based and classification based models due to the above discussed, cross-diffusion strategy and an adaptive update model. Further, in Fig. 7 we illustrate the success and precision plots of the overall performance of the tracker.

The UGF Tracker addresses the limitations of existing state-of-the-art trackers to a great extent. While, generative trackers like ASLA, IVT, and DFT were not very robust against background clutters and shape information, discriminative trackers, like WMIL, MIL, CT and STRUCK tracker were unable to

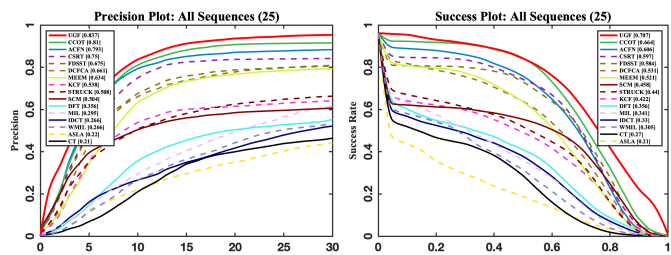


Fig. 7. Overall performance comparison of evaluated trackers: Precision Plots and Success plots. The legend ranks the trackers, using the area under curve (AUC) for the success plot, and the score at 10px threshold for the precision plot.

tackle target rotational and deformation challenges. IVT was not able to handle the dynamic appearance variations of target and DFT was not able to cater to large pose variations. KCF tracker used only a single cue for tracking and was not able to overcome variations in scale, whereas FDSST and DCFCA were unable to sustain deformations. SCM, CSRT, and CCOT showed resistance to background clutters and illumination variations but were unable to re-detect the target once the tracker drifted. CCOT had performance almost at-par with UGF but was comparatively slower.

In sum, UGF shows superior performance against state-of-the-art trackers, in both success-rate and precision threshold with highest average F-Measure, lowest average CLE and favorable computational demands on 25 benchmark videos.

V. CONCLUSION

In this paper, we have proposed UGF visual tracking framework based on multi-cue cross-diffusion involving fusion of sparse and dense similarity graphs with recursive normalization. Proposed Cross-diffusion process generates complementary feature descriptors to handle object deformations and partial occlusions. We have also introduced a robust outlier detection mechanism which is able to discard fragments with background clutter and hence ensure a clear decision boundary between positive and negative fragments. Moreover, an adaptive update methodology is proposed to efficiently handle variations in scale and illumination. Extensive qualitative and quantitative analysis on 25 sequences from OTB-50, OTB-100 and VOT2017/18 benchmark shows the effectiveness of the proposed method against state-of-the-art trackers. On average of the outcome, the proposed UGF tracker achieves 5.01 CLE, 0.829 F-Measure, success rate of 0.707, a precision score of 0.837 and accuracy of 0.748. UGF also exhibits a competitive computational time of 15.3 fps.

In future, outlier detection mechanism can be extended to have fuzzy boundaries for smoother discriminability in the proximity space, but this process is computational expensive. Another potential extension can be made by exploiting spatial relations between consecutive frames to build a holistic representation of the targeted object. Further, UGF can be extended to a multimodal environment by utilizing depth features.

REFERENCES

- [1] G. S. Walia and R. Kapoor, “Recent advances on multicue object tracking: a survey,” *Artificial Intelligence Review*, Springer, vol. 46, no. 1, pp. 1–39, 2016.

TABLE III
CENTRE LOCATION ERROR(IN PIXELS). THE BEST RESULTS ARE SHOWN IN RED, BLUE AND GREEN RESPECTIVELY.

Video	ASLA	IDCT	KCF	DFT	CT	MIL	SCM	STRUCK	WMIL	CCOT	MEEM	CSRT	FDSST	ACFN	DCFCA	Ours
Football	15.31	70.13	14.46	11.98	15.63	27.35	8.6	13.36	14.51	6.37	27.42	5.61	6.41	7.16	13.96	5.02
Walking	247.75	116.82	3.69	14.29	8.54	4.38	2.63	3.13	8.63	2.15	4.37	2.36	2.09	1.93	2.94	3.7
Subway	145.04	8.49	2.95	5.88	11.57	6.69	3.57	4.01	136.55	3.22	3.98	146.17	2.81	2.47	2.92	2.44
Jogging-2	143.99	123.05	144.68	44.01	116.98	134.42	4.24	162.07	138.35	7.18	15.22	2.47	155.17	4.55	148.57	4.22
MountainBike	21.72	15.43	7.72	10.3	192.44	7.77	10.44	12.36	110.1	10.78	13.41	8.66	8.59	9.77	8.2	5.03
Surfer	10.56	47.36	8.88	215.73	45.58	27.42	93.01	9.78	63.74	6.47	6.91	4.53	4.11	3.4	4.98	4.27
Dancer	20.01	21.21	6.29	12.34	23.2	10.81	8.49	9.36	11.63	7.17	10.06	8.31	6.75	6.55	7.29	5.64
Walking2	19.97	64.77	28.69	31.69	63.21	55.39	1.78	10.92	59.9	4.24	25.21	57.28	10.67	4.51	22.07	3.02
Boy	43.72	63.11	2.98	7.54	37.85	17.28	21.7	2.26	14.59	1.61	2.82	3.34	1.86	2.73	2.42	5.91
Dog1	27.4	16.74	4.31	41.26	6.45	7.88	7.03	3.62	6.67	4.31	5.61	4.76	2.99	3.39	4.03	3.6
Singer2	194.55	27.38	10.49	39.57	120.87	168.78	171.65	166.91	160.98	41.98	24.28	11.84	12.25	10.32	10.82	6.4
CarDark	20.31	21.32	6.16	31.51	102.98	45.31	1.06	3.41	42.54	1.51	1.22	1.23	3.15	13.33	5.25	1.22
Crossing	33.41	5.44	2.08	14.75	5.01	3.16	1.44	2.15	5.11	1.69	1.91	1.63	1.51	1.39	2.08	1.68
Fish	70.91	79.34	4.33	8.51	13.06	29.49	6.03	5.68	30.99	3.11	6.79	6.52	3.59	5.11	4.51	3.11
Car24	103.02	76.72	4.04	171.06	75.87	15.25	1.71	2.21	75.08	1.51	6.64	6.34	3.29	4.35	3.21	2.94
Bolt2	102.91	149.99	329.8	15.21	13.02	28.13	236.91	296.66	119.07	8.85	54.05	8.57	291.57	120.91	298.42	8.56
Jogging-1	99.35	15.64	88.48	34.86	92.95	95.9	60.08	122.99	94.37	4.76	6.57	6.41	102.65	4.58	89.68	9.93
BasketBall	123.37	5.51	7.73	105.14	60.16	101.74	232.7	90.4	17.1	5.7	7.21	4.62	9.86	7.65	6.25	4.60
Jumping	34.13	79.39	26.06	69.39	50.85	9.94	65.21	8.31	53.83	3.31	5.97	3.97	5.67	6.18	34.01	5.46
Bolt1	-	130.16	-	67.76	-	-	-	-	5.15	9.9	4.68	-	4.67	-	4.78	4.65
Tiger	62.61	84.41	268.11	11.57	70.27	42.71	63.51	66.83	14.28	19.86	7.29	11.04	9.71	28.31	13.27	11.02
Shaking	19.98	134.62	272.01	103.06	162.88	14.39	13.75	107.36	13.23	7.71	181.58	7.57	10.69	11.01	8.01	6.33
Singer1	4.14	20.28	11.26	24.63	33.63	22.1	4.16	14.01	2.61	39.88	2.82	2.87	3.31	16.79	12.55	4.56
Soccer1	121.81	87.96	-	112.41	80.62	36.84	152.33	110.59	5.71	92.09	57.39	11.45	39.44	84.34	21.65	4.52
Pedestrian1	96.23	23.63	47.74	119.69	79.29	27.67	73.29	7.61	39.77	6.23	6.49	4.24	40.01	8.59	20.11	5.82
Average	74.25	59.55	56.64	52.96	61.78	39.20	51.88	53.64	6.92	16.22	22.10	29.49	11.86	55.99	30.07	5.01

TABLE IV
F-MEASURE. THE BEST RESULTS ARE SHOWN IN RED, BLUE AND GREEN RESPECTIVELY.

Video	ASLA	IDCT	KCF	DFT	CT	MIL	SCM	STRUCK	WMIL	CCOT	MEEM	CSRT	FDSST	ACFN	DCFCA	Ours
Football	0.631	0.113	0.652	0.706	0.612	0.321	0.701	0.671	0.593	0.793	0.642	0.812	0.777	0.722	0.664	0.833
Walking	0.068	0.324	0.679	0.473	0.642	0.685	0.813	0.811	0.658	0.808	0.685	0.851	0.860	0.838	0.686	0.834
Subway	0.193	0.757	0.856	0.769	0.699	0.801	0.815	0.801	0.189	0.821	0.793	0.191	0.836	0.836	0.844	0.877
Jogging-2	0.133	0.152	0.142	0.27	0.091	0.138	0.849	0.151	0.133	0.815	0.711	0.883	0.144	0.867	0.139	0.891
MountainBike	0.633	0.713	0.827	0.804	0.221	0.821	0.799	0.774	0.435	0.786	0.741	0.799	0.838	0.763	0.822	0.873
Surfer	0.512	0.213	0.609	0.025	0.087	0.198	0.036	0.651	0.038	0.728	0.655	0.669	0.815	0.821	0.666	0.811
Dancer	0.631	0.703	0.779	0.745	0.662	0.751	0.783	0.811	0.732	0.874	0.768	0.849	0.874	0.853	0.773	0.881
Walking2	0.464	0.334	0.511	0.506	0.314	0.315	0.894	0.652	0.343	0.848	0.325	0.391	0.767	0.841	0.594	0.879
Boy	0.316	0.576	0.871	0.763	0.458	0.501	0.653	0.874	0.559	0.924	0.877	0.868	0.919	0.848	0.882	0.807
Dog1	0.528	0.604	0.868	0.442	0.662	0.657	0.834	0.893	0.655	0.886	0.672	0.867	0.924	0.753	0.673	0.672
Singer2	0.052	0.699	0.841	0.561	0.137	0.048	0.055	0.054	0.063	0.042	0.054	0.835	0.811	0.772	0.836	0.855
CarDark	0.55	0.371	0.749	0.492	0.03	0.215	0.925	0.743	0.258	0.916	0.923	0.923	0.86	0.665	0.781	0.929
Crossing	0.379	0.736	0.825	0.615	0.781	0.837	0.884	0.842	0.661	0.872	0.828	0.867	0.893	0.889	0.829	0.878
Fish	0.171	0.147	0.911	0.854	0.774	0.519	0.868	0.885	0.471	0.926	0.875	0.876	0.905	0.886	0.909	0.921
Car24	0.198	0.350	0.581	0.113	0.325	0.638	0.933	0.899	0.313	0.945	0.582	0.581	0.704	0.779	0.578	0.911
Bolt2	0.023	0.162	0.014	0.699	0.644	0.326	0.013	0.019	0.386	0.632	0.013	0.732	0.014	0.016	0.014	0.781
Jogging-1	0.16	0.767	0.207	0.221	0.191	0.158	0.203	0.188	0.137	0.877	0.781	0.822	0.207	0.891	0.204	0.695
BasketBall	0.164	0.881	0.797	0.285	0.401	0.258	0.095	0.382	0.681	0.807	0.822	0.675	0.751	0.576	0.853	0.834
Jumping	0.176	0.071	0.339	0.031	0.055	0.668	0.049	0.707	0.049	0.807	0.782	0.834	0.729	0.729	0.579	0.791
Bolt1	0.008	0.276	0.007	0.078	0.03	0.012	0.009	0.008	0.773	0.731	0.823	0.012	0.656	0.014	0.861	0.839
Tiger	0.13	0.251	0.013	0.813	0.191	0.499	0.308	0.262	0.729	0.679	0.821	0.807	0.748	0.587	0.786	0.814
Shaking	0.323	0.02	0.007	0.236	0.051	0.726	0.754	0.08	0.767	0.831	0.052	0.848	0.783	0.781	0.821	0.858
Singer1	0.29	0.44	0.476	0.441	0.347	0.456	0.912	0.478	0.931	0.394	0.927	0.888	0.843	0.472	0.476	0.912
Soccer1	0.059	0.302	0.055	0.211	0.197	0.355	0.128	0.156	0.766	0.219	0.258	0.663	0.306	0.182	0.494	0.688
Pedestrian1	0.055	0.434	0.231	0.02	0.236	0.099	0.086	0.601	0.526	0.741	0.734	0.754	0.53	0.727	0.527	0.761
Average	0.285	0.416	0.514	0.447	0.354	0.440	0.536	0.536	0.792	0.645	0.718	0.695	0.736	0.397	0.652	0.829

- [2] W. Xue, C. Xu, and Z. Feng, "Robust visual tracking via multi-scale spatio-temporal context learning," *IEEE Transactions on Circuits and Systems for Video Technology*, 2017.
- [3] J. Fang, H. Xu, Q. Wang, and T. Wu, "Online hash tracking with spatio-temporal saliency auxiliary," *Computer Vision and Image Understanding*, vol. 160, pp. 57–72, 2017.
- [4] X. Lan, A. J. Ma, P. C. Yuen, and R. Chellappa, "Joint sparse representation and robust feature-level fusion for multi-cue visual tracking," *IEEE Tran. on Image Processing*, vol. 24, no. 12, pp. 5826–5841, 2015.
- [5] A. Lukežič, L. Č. Zajc, and M. Kristan, "Deformable parts correlation filters for robust visual tracking," *IEEE transactions on cybernetics*, vol. 48, no. 6, pp. 1849–1861, 2018.
- [6] L. Sevilla-Lara and E. Learned-Miller, "Distribution fields for tracking," in *IEEE Conference on Computer vision and pattern recognition (CVPR)*, pp. 1910–1917, 2012.
- [7] X. Jia, H. Lu, and M.-H. Yang, "Visual tracking via adaptive structural local sparse appearance model," in *IEEE Conference on Computer vision and pattern recognition (CVPR)*, pp. 1822–1829, 2012.
- [8] B. Babenko, M.-H. Yang, and S. Belongie, "Robust object tracking with online multiple instance learning," *IEEE transactions on pattern analysis and machine intelligence*, vol. 33, no. 8, pp. 1619–1632, 2011.
- [9] S. Hare, S. Golodetz, A. Saffari, V. Vineet, M.-M. Cheng, S. L. Hicks, and P. H. Torr, "Struck: Structured output tracking with kernels," *IEEE Tran. Patt. Anal. Mach. Intell.*, vol. 38, no. 10, pp. 2096–2109, 2016.
- [10] K. Zhang, L. Zhang, and M.-H. Yang, "Real-time compressive tracking," in *European conf. on computer vision*, pp. 864–877, Springer, 2012.
- [11] J. Gao, T. Zhang, X. Yang, and C. Xu, "Deep relative tracking," *IEEE Transactions on Image Processing*, vol. 26, no. 4, pp. 1845–1858, 2017.
- [12] Y. Qi, S. Zhang, L. Qin, Q. Huang, H. Yao, J. Lim, and M.-H. Yang, "Hedging deep features for visual tracking," *IEEE Transactions on*

- Pattern Analysis and Machine Intelligence*, 2018.
- [13] J. Gao, T. Zhang, X. Yang, and C. Xu, "P2t: Part-to-target tracking via deep regression learning," *IEEE Transactions on Image Processing*, vol. 27, no. 6, pp. 3074–3086, 2018.
 - [14] Z. Li, J. Zhang, K. Zhang, and Z. Li, "Visual tracking with weighted adaptive local sparse appearance model via spatio-temporal context learning," *IEEE Transactions on Image Processing*, 2018.
 - [15] Z. Chen, X. You, B. Zhong, J. Li, and D. Tao, "Dynamically modulated mask sparse tracking," *IEEE trans. cybernetics*, vol. 47, 2017.
 - [16] K. Nai, Z. Li, G. Li, and S. Wang, "Robust object tracking via local sparse appearance model," *IEEE Trans. on Image Processing*, 2018.
 - [17] Y. Qi, L. Qin, J. Zhang, S. Zhang, Q. Huang, and M.-H. Yang, "Structure-aware local sparse coding for visual tracking," *IEEE Transactions on Image Processing*, vol. 27, no. 8, pp. 3857–3869, 2018.
 - [18] L. Huang, B. Ma, J. Shen, H. He, L. Shao, and F. Porikli, "Visual tracking by sampling in part space," *IEEE Transactions on Image Processing*, vol. 26, no. 12, pp. 5800–5810, 2017.
 - [19] B. Fan, Y. Cong, and Y. Tang, "Dual graph regularized discriminative multi-task tracker," *IEEE Transactions on Multimedia*, 2018.
 - [20] D. Du, H. Qi, L. Wen, Q. Tian, Q. Huang, and S. Lyu, "Geometric hypergraph learning for visual tracking," *IEEE transactions on cybernetics*, vol. 47, no. 12, pp. 4182–4195, 2017.
 - [21] Y. Sui, G. Wang, and L. Zhang, "Correlation filter learning toward peak strength for visual tracking," *IEEE transactions on cybernetics*, vol. 48, no. 4, pp. 1290–1303, 2018.
 - [22] H. Hu, B. Ma, J. Shen, and L. Shao, "Manifold regularized correlation object tracking," *IEEE transactions on neural networks and learning systems*, vol. 29, no. 5, pp. 1786–1795, 2018.
 - [23] D. Du, L. Wen, H. Qi, Q. Huang, Q. Tian, and S. Lyu, "Iterative graph seeking for object tracking," *IEEE Transactions on Image Processing*, vol. 27, no. 4, pp. 1809–1821, 2018.
 - [24] L. Wang, L. Zhang, and Z. Yi, "Trajectory predictor by using recurrent neural networks in visual tracking," *IEEE transactions on cybernetics*, vol. 47, no. 10, pp. 3172–3183, 2017.
 - [25] E. Gundogdu and A. A. Alatan, "Good features to correlate for visual tracking," *IEEE Transactions on Image Processing*, vol. 27, no. 5, pp. 2526–2540, 2018.
 - [26] L. Zhang and P. N. Suganthan, "Visual tracking with convolutional random vector functional link network," *IEEE transactions on cybernetics*, vol. 47, no. 10, pp. 3243–3253, 2017.
 - [27] B. K. Horn and B. G. Schunck, "Determining optical flow," *Artificial intelligence*, vol. 17, no. 1-3, pp. 185–203, 1981.
 - [28] T. Ojala, M. Pietikainen, and T. Maenpaa, "Multiresolution gray-scale and rotation invariant texture classification with local binary patterns," *IEEE Tran. patt. ana. and mach. intell.*, pp. 971–987, 2002.
 - [29] N. Dalal and B. Triggs, "Histograms of oriented gradients for human detection," in *Comp. Vis. and Pattern Recog., IEEE Computer Society Conference*, vol. 1, pp. 886–893, 2005.
 - [30] B. Wang, J. Jiang, W. Wang, Z.-H. Zhou, and Z. Tu, "Unsupervised metric fusion by cross diffusion," in *IEEE Conference on Computer Vision and Pattern Recognition (CVPR)*, pp. 2997–3004, 2012.
 - [31] T. Tong, K. Gray, Q. Gao, L. Chen, D. Rueckert, A. D. N. Initiative, et al., "Multi-modal classification of alzheimer's disease using nonlinear graph fusion," *Pattern recognition*, vol. 63, pp. 171–181, 2017.
 - [32] L. Breiman, J. Friedman, C. J. Stone, and R. A. Olshen, *Classification and regression trees*. CRC press, 1984.
 - [33] B. Schölkopf and A. J. Smola, *Learning with kernels: support vector machines, regularization, optimization, and beyond*. MIT press, 2002.
 - [34] Y. Wu, J. Lim, and M.-H. Yang, "Object tracking benchmark," *IEEE Transactions on Pattern Analysis and Machine Intelligence*, vol. 37, no. 9, pp. 1834–1848, 2015.
 - [35] M. Kristan, J. Matas, and A. L. et. al., "A novel performance evaluation methodology for single-target trackers," *IEEE Trans. on Pattern Analysis and Machine Intell.*, vol. 38-11, pp. 2137–55, 2016.
 - [36] K. Zhang and H. Song, "Real-time visual tracking via online weighted multiple instance learning," *Pattern Recog.*, vol. 46, pp. 397–411, 2013.
 - [37] A. Asvadi, H. Mahdavinataj, M. R. Karami, and Y. Baleghi, "Online visual object tracking using incremental discriminative color learning," *The CSI Journal on Comp. Sc. and Engg.*, 2014.
 - [38] M. Danelljan, G. Häger, F. S. Khan, and M. Felsberg, "Discriminative scale space tracking," *IEEE transactions on pattern analysis and machine intelligence*, vol. 39, no. 8, pp. 1561–1575, 2017.
 - [39] M. Danelljan, A. Robinson, F. S. Khan, and M. Felsberg, "Beyond correlation filters: Learning continuous convolution operators for visual tracking," in *Euro. Conf. on Comp. Vis.*, pp. 472–488, Springer, 2016.
 - [40] J. Zhang, S. Ma, and S. Sclaroff, "Meem: robust tracking via multiple experts using entropy minimization," in *European Conference on Computer Vision*, pp. 188–203, Springer, 2014.
 - [41] A. Lukezic, T. Vojir, L. C. Zajc, J. Matas, and M. Kristan, "Discriminative correlation filter with channel and spatial reliability," in *CVPR*, vol. 6, p. 8, 2017.
 - [42] J. Choi, H. J. Chang, S. Yun, T. Fischer, Y. Demiris, J. Y. Choi, et al., "Attentional correlation filter network for adaptive visual tracking," in *CVPR*, vol. 2, p. 7, 2017.
 - [43] M. Mueller, N. Smith, and B. Ghanem, "Context-aware correlation filter tracking," in *Proc. of the IEEE Conference on Computer Vision and Pattern Recognition (CVPR)*, vol. 2, p. 6, 2017.
 - [44] J. F. Henriques, R. Caseiro, P. Martins, and J. Batista, "High-speed tracking with kernelized correlation filters," *IEEE Trans. on Pattern Analysis and Machine Intelligence*, vol. 37, no. 3, pp. 583–596, 2015.
 - [45] W. Zhong, H. Lu, and M.-H. Yang, "Robust object tracking via sparsity-based collaborative model," in *IEEE Conference on Computer vision and pattern recognition (CVPR)*, pp. 1838–1845, 2012.